Near-field thermal radiation transfer between semiconductors based on thickness control and introduction of photonic crystals

Takuya Inoue,* Takashi Asano, and Susumu Noda
Department of Electronic Science and Engineering, Kyoto University, Kyoto-Daigaku-Katsura, Nishikyo-ku, Kyoto 615-8510, Japan
(Received 22 November 2016; revised manuscript received 27 January 2017; published 9 March 2017)

We numerically investigate the spectral control of near-field thermal radiation transfer using interband absorption in semiconductors and the band-folding effect in photonic crystals (PCs) for highly efficient thermophotovoltaics. We reveal that the near-field coupling between two semiconductors (Si and GaSb) realizes frequency-selective thermal radiation transfer concentrated above their bandgap energy when their thicknesses are optimized considering their absorption coefficient spectra. Moreover, we elucidate the role of PC structures in the near-field thermal radiation transfer and demonstrate that the band-folding effect in PCs can further increase both the radiation power and frequency selectivity of the near-field thermal radiation transfer.

DOI: 10.1103/PhysRevB.95.125307

I. INTRODUCTION

It is well known that evanescent coupling of light between two objects greatly enhances the thermal radiation transfer between them [1–3]. This phenomenon is called near-field thermal radiation transfer (or near-field radiative heat transfer) and is attracting increasing attention for a number of applications such as thermophotovoltaics (TPVs) [4–8] and thermal rectification [9,10]. So far, many papers have numerically reported a great enhancement in net radiative heat transfer in the near-field regime using planar or nanostructured materials [11–18]. However, fewer studies have focused on the suppression of unnecessary near-field thermal radiation transfer outside the target wavelengths, although it is very important in many applications. For example, in the near-field TPV application, the radiation transfer below the bandgap energy of photovoltaic cells leads to the decrease of the power conversion efficiency (the electric power generated for a given input heating power) as well as unwanted heating of solar cells, which deteriorates the electrical characteristics of the cells.

In this paper, we investigate a method of realizing near-field thermal radiation transfer concentrated in a target wavelength range, while suppressing it at other wavelengths. We have previously demonstrated the spectral control of thermal emission in the far-field regime via the simultaneous control of the materials' absorption coefficient spectra and photonic density of states inside an emitter [19–21]. Based on this concept, here, we realize near-field narrowband thermal radiation transfer in the near-infrared region for highly efficient TPV. We specifically focus on the near-field thermal radiation transfer between a Si emitter and a GaSb absorber because both materials show large absorption coefficients in the near-infrared range and are thus expected to yield frequency-selective thermal radiation transfer. Furthermore, we introduce a photonic crystal (PC) structure into the emitter and utilize its band-folding effect to further enhance the thermal radiation transfer in the near-infrared range, while suppressing it at longer wavelengths.

The paper is organized as follows. In Sec. II, we present numerical simulations of the near-field thermal radiation transfer between a Si planar emitter and a GaSb planar absorber. We demonstrate that the frequency-selective thermal radiation transfer, which concentrates above the materials' bandgap energy, can be obtained when their thicknesses are optimized considering the materials' absorption coefficient spectra. In Sec. III, we discuss the role of PC structures in the near-field thermal radiation transfer and demonstrate that the selective diffraction of light with the above-bandgap energy owing to the band-folding effect increases both the radiation power and frequency selectivity.

II. NEAR-FIELD THERMAL RADIATION TRANSFER BETWEEN SI AND GASB SLABS WITHOUT PCS

A. Simulation model

We consider the system shown in Fig. 1(a), where an undoped Si emitter (with a thickness of t_1) and an n-doped GaSb absorber (with a thickness of t_2 and a doping density of $1.0 \times 10^{17}\,\mathrm{cm}^{-3}$) are separated by a vacuum gap (with a thickness of d). We assume the emitter's temperature to be 1400 K, which is below the melting point of silicon ($\sim$1680 K), and the absorber's temperature to be 300 K. The real part of the permittivity and the absorption coefficients of the two materials are shown in Figs. 1(b) and 1(c), respectively. Here, we take account of the temperature dependence of the refractive index, bandgap energy, and free carrier density of Si [11,22]. The bandgap energy of silicon decreases from 1.1 eV at 300 K to 0.7 eV at 1400 K [22]. This agrees well with the bandgap energy of GaSb, as shown in Fig. 1(c), and thus, it is expected to yield an enhanced thermal radiation transfer in the above-bandgap energy. The optical constant of GaSb is taken from Refs. [23,24]. To discuss the frequency selectivity of the thermal radiation transfer in typical photovoltaic cells, we assume that n-doped GaSb is used instead of undoped GaSb and take account of below-bandgap thermal radiation transfer caused by free carriers in the emitter and absorber.

For the calculation of the near-field thermal radiation transfer between the two parallel slabs (with PC structures in Sec. III), we develop a simulation method based on the fluctuation-dissipation theory [25] and the rigorous coupled wave analysis (RCWA) [26]. The details of the method are described in Appendix A. In the following, we calculate the near-field thermal radiation power absorbed by the GaSb slab and the far-field radiation loss transmitted through the GaSb slab.

*t_inoue@qoe.kuee.kyoto-u.ac.jp

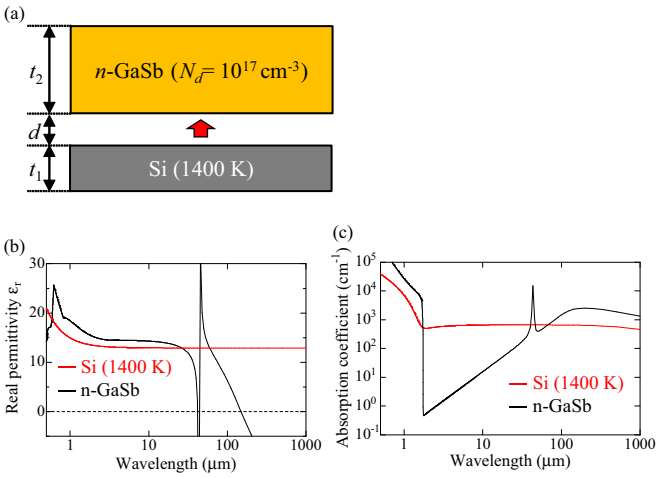

FIG. 1. (a) Simulation model of the near-field thermal radiation transfer between Si and GaSb. (b) Real part of the permittivity of Si at 1400 K and n-type GaSb at 300 K. (c) Absorption coefficient of Si at 1400 K and n-type GaSb at 300 K.

B. Results

Here, we show the calculation results of the near-field thermal radiation transfer in the abovementioned model and discuss the dependence of the frequency selectivity on the gap and thicknesses of the emitter and absorber.

In the first case, we assume a semi-infinite Si/GaSb substrate ($t_1 = t_2 = \infty$) and calculate the evolution of the near-field thermal radiation transfer spectra between the two substrates while decreasing vacuum gaps (d). The results are shown in Figs. 2(a)–2(d). When the gap is relatively large [Fig. 2(a)], the absorption spectrum of GaSb (red line) is broadband like blackbody emission, which is due to infinite interaction of light and matter inside the semi-infinite Si/GaSb substrate. As the gap is decreased, the free carrier absorption at longer wavelengths is first enhanced [Fig. 2(b)], followed by the enhancement of the above-bandgap absorption [Fig. 2(c)]. The degree of the absorption enhancement compared to the far-field blackbody limit (black line) at wavelengths of $1 - 20\,\mu$m is about 12 times greater, which is equal to the square of the refractive index of Si [11]. This enhancement comes from the increase of the photonic density of states inside a high-refractive-index object compared to that inside vacuum. However, when the gap is very small [Fig. 2(d)], a much larger enhancement of absorption is obtained at wavelengths longer than $20\,\mu$m. Such a large thermal radiation transfer is caused by surface waves at the interface, which are supported by the negative permittivity of n-doped GaSb, as shown in Fig. 1(b). Figure 2(e) shows the total absorption power (black line) and the absorption above and below the bandgap energy of GaSb (red line and blue line, respectively) as functions of the vacuum gap. When the gap is smaller than $0.2\,\mu$m, the above-bandgap absorption power exceeds the far-field limit (red dashed line), which leads to the enhancement of the generated electrical power in the case of TPV applications. However, in such applications, it is also important to suppress the below-bandgap absorption and maximize the ratio of the above-bandgap absorption to the total emission power.

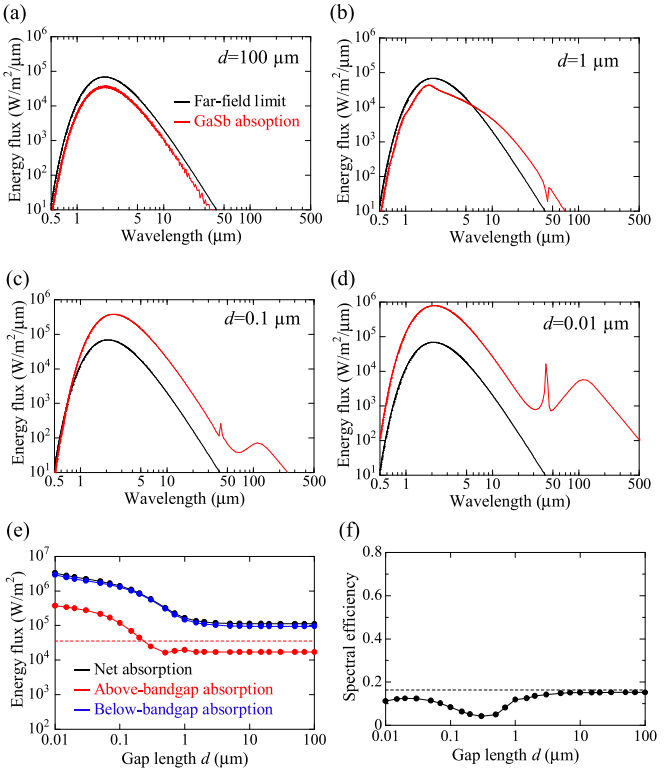

FIG. 2. (a)–(d) Calculated near-field thermal radiation transfer spectra between a semi-infinite Si substrate and a semi-infinite GaSb substrate with various vacuum gaps. (e) Absorption of GaSb as a function of the vacuum gap. (f) SE as a function of the vacuum gap. The dashed line shows the SE of a far-field blackbody.

Therefore, we define the spectral efficiency (SE) of the system by the following equations:

$$\mathrm{SE} = \frac{P_{\mathrm{above}-E_g}}{P_{\mathrm{above}-E_g} + P_{\mathrm{below}-E_g} + P_{\mathrm{transmission}}}, \qquad (1)$$

where $P_{\mathrm{above}-E_g}$, $P_{\mathrm{below}-E_g}$, $P_{\mathrm{transmission}}$ are above-bandgap absorption power in GaSb, below-bandgap absorption power in GaSb, and transmission loss (zero in the semi-infinite case), respectively. Although we can directly calculate the generated electric power and power generation efficiency by assuming a specific structure of a photovoltaic cell, here, we focus on SE in order to discuss general methods for realizing frequency-selective near-field thermal radiation transfer and to reveal the underlying physics behind them. Figure 2(f) shows the calculated SE as a function of the gap. The dashed line shows the SE of a far-field blackbody. As seen in the figure, the SE never exceeds the far-field value. This is because not only the above-bandgap absorption but also the below-bandgap absorption is significantly enhanced in the case of semi-infinite substrates.

Next, we calculate the thermal radiation transfer between the Si and GaSb slabs with finite thicknesses ($t_1 = t_2 = 2\,\mu$m). The calculated absorption spectra (red line) and the transmission spectra (gray line) of the GaSb slab are shown in Figs. 3(a)–3(d). Unlike the semi-infinite case (Fig. 2), almost all of the below-bandgap emission from the Si emitter passes through GaSb when the gap is large [Fig. 3(a)], and

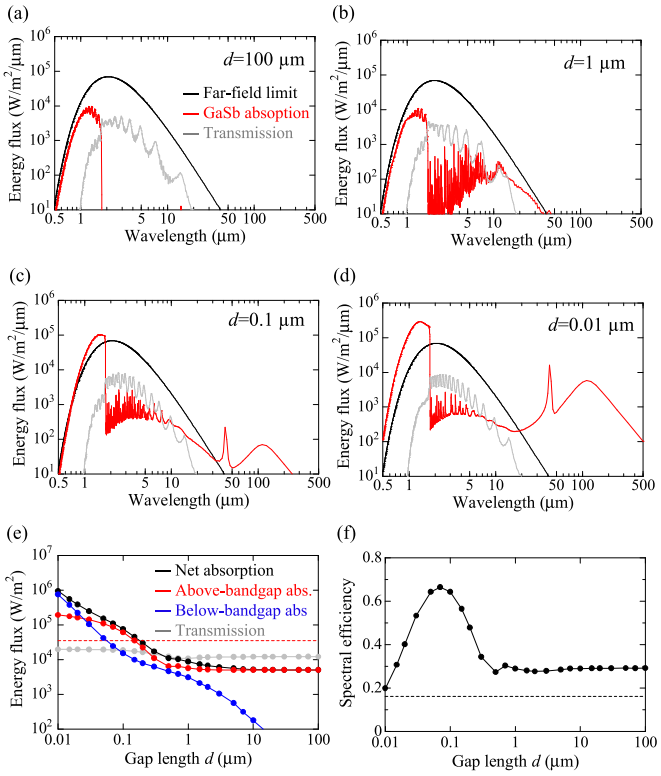

FIG. 3. (a)–(d) Calculated near-field thermal radiation transfer spectra between a thin Si slab ($t_1 = 2\,\mu$m) and a thin GaSb slab ($t_2 = 2\,\mu$m) with various vacuum gaps. (e) Absorption and transmission power of GaSb as functions of the vacuum gap. (f) SE as a function of the vacuum gap. The dashed line shows the SE of a far-field blackbody.

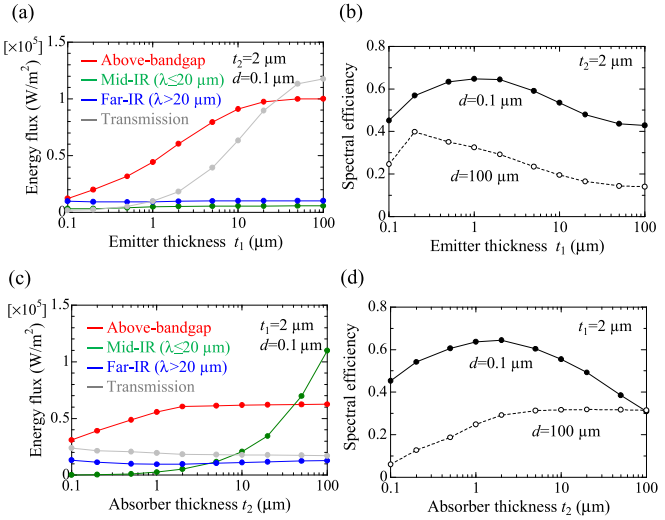

FIG. 4. (a) Calculated energy flux of the near-field thermal radiation as a function of the emitter thickness. The red, green, and blue lines show the GaSb absorption in the near-infrared, mid-infrared, and far-infrared regions. The gray line shows the transmission power through the absorber. The gap and the absorber thickness are set to $d = 0.1\,\mu$m and $t_2 = 2\,\mu$m, respectively. (b) Calculated SE as a function of the emitter thickness. Solid line: $d = 0.1\,\mu$m, dashed line: $d = 100\,\mu$m. (c) Calculated energy flux of the near-field thermal radiation as a function of the absorber thickness. The gap and the emitter thickness are set to $d = 0.1\,\mu$m and $t_1 = 2\,\mu$m, respectively. (d) SE as a function of the absorber thickness. Solid line: $d = 0.1\,\mu$m, dashed line: $d = 100\,\mu$m.

the situation does not change much even when the gap is reduced to $1 - 0.1\,\mu$m [Figs. 3(b) and 3(c)]. On the other hand, the above-bandgap absorption of GaSb is significantly enhanced like in the semi-infinite case, and consequently, the frequency-selective thermal radiation transfer is achieved at a gap of $0.1\,\mu$m [Fig. 3(c)]. These results come from the fact that both Si and GaSb have a large absorption coefficient only in the near-infrared range, as shown in Fig. 1(c). Figure 3(e) shows the total absorption power (black line), absorption above and below the bandgap energy of GaSb (red line and blue line, respectively), and transmission power (gray line) as functions of the vacuum gap. By reducing the vacuum gap to $0.1 - 0.2\,\mu$m, we can achieve the above-bandgap absorption exceeding the far-field blackbody limit while keeping the below-bandgap absorption much smaller. The light transmitted through the absorber propagates to the far field and is thus not enhanced by the near-field coupling of the emitter and absorber, even when the gap becomes small. The calculated SE is shown in Fig. 3(f). We can dramatically improve the SE compared to the far-field value by reducing the gap to around $0.1\,\mu$m. The decrease in the SE at a gap thickness below $0.05\,\mu$m is caused by a significant increase in the below-bandgap thermal radiation transfer mediated by surface waves, as shown in Fig. 3(d).

The increased frequency selectivity demonstrated in Fig. 3 results from the proper choice of the thicknesses of the emitter and absorber. Figures 4(a) and 4(b) show the calculated energy flux of the near-field thermal radiation and its SE as functions of the emitter thickness. In Fig. 4(a), the gap thickness is set to $d = 0.1\,\mu$m [near the maximum point in Fig. 3(f)], and the absorber thickness is set to $t_2 = 2\,\mu$m. When the emitter thickness is too large, the below-bandgap transmission through the absorber (gray line) exceeds the above-bandgap absorption (red line) and decreases the SE, which is due to the broadband emission by free carriers inside Si. More quantitatively, the below-bandgap absorption coefficient of Si at 1400 K in Fig. 1(c) is approximately $660\,\mathrm{cm}^{-1} = (15\,\mu\mathrm{m})^{-1}$, and thus, the emitter thickness should be reduced to below $15\,\mu$m to achieve the frequency selective thermal radiation transfer. However, if the emitter thickness is too small, the above-bandgap radiation transfer is insufficient compared to the thickness-independent far-infrared thermal radiation transfer (blue line) caused by surface waves. Therefore, the SE at $d = 0.1\,\mu$m is maximized when the emitter thickness is approximately $t_1 = 1 - 2\,\mu$m, as shown in Fig. 4(b) (solid line). A similar tendency applies to the absorber thickness dependence of the near-field thermal radiation transfer shown in Figs. 4(c) and 4(d). When the absorber is too thick ($>5\,\mu$m), the mid-infrared free carrier absorption in n-GaSb (green line) exponentially increases, while the above-bandgap absorption saturates. When the absorber is too thin, the transmission loss becomes dominant. Therefore, to maximize the SE at $d = 0.1\,\mu$m, the absorber thickness should be also $t_2 = 1 - 2\,\mu$m. The optimum thicknesses of the emitter and absorber in the near-field case are different from those in the far-field case

($d = 100\,\mu$m), where thinner emitters and thicker absorbers lead to a higher SE, as indicated with dashed lines in Figs. 4(b) and 4(d).

III. NEAR-FIELD THERMAL RADIATION TRANSFER BETWEEN SI AND GASB SLABS WITH PCS

In this section, we present the spectral control of the near-field thermal radiation transfer using a PC slab. The use of the PC slab has been successful for the spectral control of the thermal radiation spectrum in the far-field range [19–21], in which the quasiguiding modes supported by the periodic structures achieve the efficient diffraction of thermal emission into free space owing to the band-folding effect at the resonant frequencies. However, in the case of the near-field thermal radiation transfer, the diffraction might not necessarily lead to the enhancement of the radiation transfer because the guided modes confined inside the slab can directly couple to the absorber via the evanescent waves. Therefore, the purpose of the calculations provided in this section is to clarify the role of PCs in the near-field thermal radiation transfer and to find a PC structure that can further enhance the frequency selectivity of the near-field thermal radiation transfer.

The calculation model is shown in Fig. 5(a), where a one-dimensional Si PC slab with a period of a and a stripe width of w (1400 K) is separated from an n-doped GaSb absorber (300 K). Here, the thicknesses of both the emitter and absorber

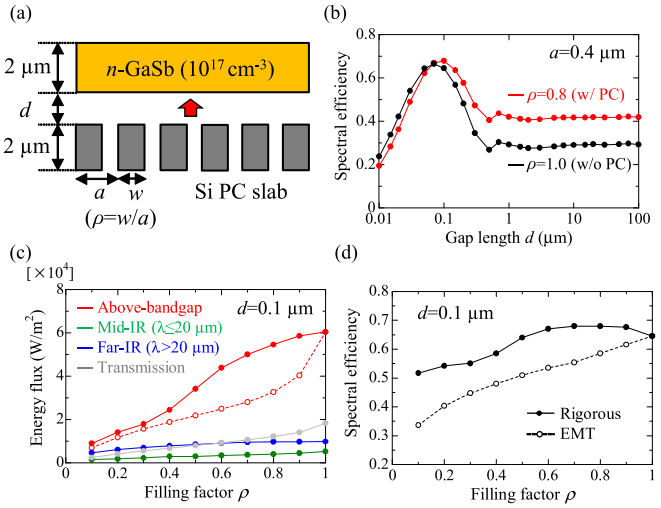

FIG. 5. (a) Simulation model of the near-field thermal radiation transfer between a Si PC emitter and a GaSb absorber. (b) Calculated spectral efficiencies with and without a PC as functions of the vacuum gap. The lattice constant of the PC is set to $a = 0.4\,\mu$m. (c) Calculated energy flux of the near-field thermal radiation as a function of the filling factor. The red, green, and blue lines show the GaSb absorption in the near-infrared, mid-infrared, and far-infrared regions. The gray line shows the transmission power through the absorber. The dashed red line shows the above-bandgap GaSb absorption calculated by the EMT, which does not take account of the light diffraction. The difference between the solid line and the dashed line suggests that the band-folding effect in the PC does enhance the above-bandgap thermal radiation transfer. (d) Calculated SE as a function of the filling factor at $d = 0.1\,\mu$m.

are set to $2\,\mu$m, where the maximum SE is obtained in the previous section (Fig. 4).

First, we fix the lattice constant of the PC to $0.4\,\mu$m and calculate the SE of the near-field thermal radiation transfer by varying the PC filling factor ($\rho = w/a$). The results are shown in Fig. 5(b). In the far-field regime ($d > 1\,\mu$m), the SE with the PC ($\rho = 0.8$, red line) becomes higher than that without a PC ($\rho = 1$, black line) owing to the efficient diffraction of thermal emission to the far field as we have mentioned above. However, when the gap is very small ($d \sim 0.01\,\mu$m), the SE with the PC becomes lower than that without a PC. In this regime, the presence of the light diffraction (band folding) does not influence the thermal radiation transfer because every guided mode inside the emitter can couple to the absorber owing to the sufficiently small gap. In this case, the above-bandgap absorption inside the absorber is simply determined by the photonic density of states inside the Si emitter. The photonic density of states inside the PC structure is smaller than that inside the planar emitter due to the lower effective refractive index, which leads to the reduction of the above-bandgap absorption power. The most important point we should discuss here is the enhancement of the maximum SE with the PC structure at a moderately small gap ($d = 0.1\,\mu$m). Figures 5(c) and 5(d) (solid lines) show the calculated energy flux of the near-field thermal radiation and its SE as functions of the filling factor at $d = 0.1\,\mu$m. In Fig. 5(c), both the above-bandgap absorption and below-bandgap losses (absorption and transmission) monotonically decrease with ρ, but the former decreases slower than the latter, which leads to the maximum SE around $\rho = 0.8$, as shown in Fig. 5(d).

Let us explain the physical reasons behind the results shown in Figs. 5(c) and 5(d). At a moderately small gap, both the diffraction of thermal emission owing to the band-folding effect and the decrease of the photonic density of states can influence the thermal radiation transfer: the former can increase the energy flux, while the latter decreases the energy flux. To separate these two effects, we perform the calculation of the near-field thermal radiation transfer using the effective medium theory (EMT), where a one-dimensional PC slab is approximated with a uniform slab having an anisotropic effective permittivity

$$\varepsilon_{//} = \varepsilon_{\mathrm{Si}}\rho + \varepsilon_{\mathrm{air}}(1-\rho)$$
$$\varepsilon_{\perp} = \left[\varepsilon_{\mathrm{Si}}^{-1}\rho + \varepsilon_{\mathrm{air}}^{-1}(1-\rho)\right]^{-1}. \quad (2)$$

Here, $\varepsilon_{//}$ and $\varepsilon_{\perp}$ denote the permittivities for electric fields parallel and vertical to the stripes. The EMT does not take account of the light diffraction but only takes account of the change of the photonic density of states. The calculated above-bandgap GaSb absorption power and SE are superimposed in Figs. 5(c) and 5(d) with dashed lines. Here, the above-bandgap absorption calculated by the EMT rapidly decreases with ρ. The difference between the solid lines and the dashed lines in Fig. 5(c) suggests that the band-folding effect in the PC does enhance the above-bandgap thermal radiation transfer even at a moderately small gap of $d = 0.1\,\mu$m. On the other hand, the below-bandgap losses calculated by the EMT (not shown) is almost equal to that calculated by the rigorous method, which suggests that the period of the PC ($a = 0.4\,\mu$m) is too

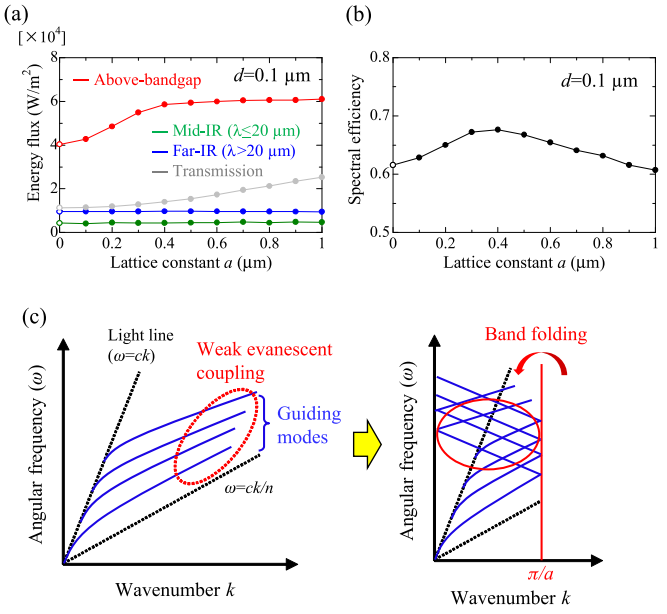

FIG. 6. (a) Calculated energy flux of the near-field thermal radiation as a function of the lattice constant. The red, green, and blue lines show the GaSb absorption in the near-infrared, mid-infrared, and far-infrared regions. The gray line shows the transmission power through the absorber. (b) Calculated SE as a function of the lattice constant at $d = 0.1\ \mu$m. (c) Schematic diagram for the enhancement of the near-field thermal radiation transfer by the band-folding effect of PCs. Left: dispersion diagram for the guiding modes inside a flat slab. Right: dispersion diagram for the guiding modes inside a PC slab.

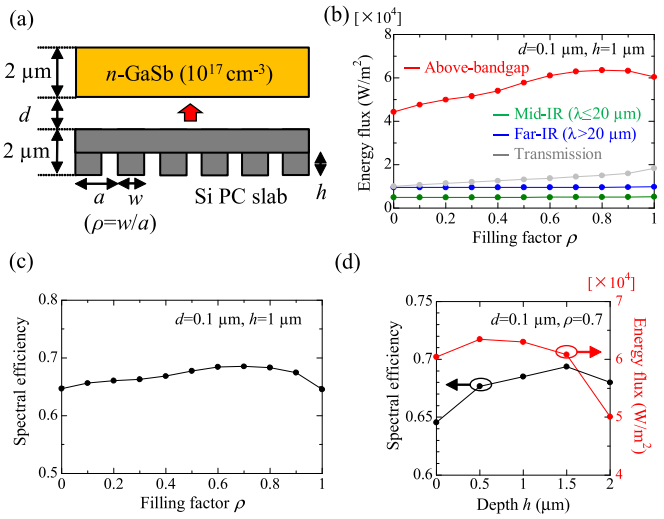

FIG. 7. (a) Simulation model of the near-field thermal radiation transfer between a Si PC emitter with partially etched stripes and a GaSb absorber. The designed PC emitter has a flat upper surface to mitigate the decrease of the photonic density of states, while the strength of the diffraction can be adjusted with the filling factor and the depth of the stripes at the backside. (b) Calculated energy flux of the near-field thermal radiation as a function of the filling factor. The stripe depth is set to 1 μm. The red, green, and blue lines show the GaSb absorption in the near-infrared, mid-infrared, and far-infrared regions. The gray line shows the transmission power through the absorber. (c) Calculated SE as a function of the filling factor at $d = 0.1\ \mu$m and $h = 1\ \mu$m. (d) SE (black line) and above-bandgap GaSb absorption power (red line) of the near-field thermal radiation as functions of the stripe depth at $d = 0.1\ \mu$m and $\rho = 0.7$.

small to induce the diffraction of mid-infrared and far-infrared emission (the details are discussed later). Therefore, the band-folding effect in the PC structure selectively increases the above-bandgap thermal emission, which also increases the SE as shown in the difference between the solid lines and the dashed lines in Fig. 5(d).

To further investigate the role of band folding, we perform the same calculations by varying the lattice constant of the PC with the fixed filling factor ($\rho = 0.9$). The results are shown in Figs. 6(a) and 6(b), where the limit as the lattice constant goes to zero is calculated by the EMT. As the lattice constant increases, the above-bandgap absorption increases at first, and then the transmission loss increases. This result can be qualitatively explained as follows. The left panel of Fig. 6(c) shows the schematic diagram of the dispersion curves of the guiding modes inside a flat slab without a PC structure. Among these guiding modes, the ones far away from the light line ($\omega = ck$) contribute less to the near-field thermal radiation transfer since they are strongly confined inside the slab and evanescent coupling is weak. When the PC structure is introduced in the slab, these modes are brought above or near the light lines by the band-folding effect of the PC and contribute to the enhancement of the thermal radiation transfer [right panel in Fig. 6(c)]. By choosing the lattice constant properly ($a \sim 0.4\ \mu$m), we can selectively enhance the thermal radiation transfer in the above-bandgap energy. However, if the lattice constant is too large [the magnitude of the reciprocal vectors of the PC ($2\pi/a$) is too small], the band folding is induced at lower frequencies, which decreases the frequency selectivity of the thermal radiation transfer. More quantitative results are described in Appendix B.

So far, we have demonstrated that the introduction of a PC structure to the emitter can increase the SE of the near-field thermal radiation transfer. For example, in Fig. 5(d), the SE without a PC structure (64.5%) becomes 68.0% with the PC structure ($\rho = 0.8$). However, in Fig. 5(c), the absolute value of the above-bandgap absorption with the PC structure ($\rho = 0.8$) becomes smaller than that without a PC structure by $\sim$10%, which is due to the decrease of the photonic density of states inside the PC emitter. To realize the simultaneous increase of the SE and the absolute value of the absorption power, we investigate a one-dimensional PC with partially etched stripes, as shown in Fig. 7(a). Since the evanescent coupling between the emitter and the absorber is dominant near the upper surface, the designed PC structure has a flat upper surface to mitigate the decrease of the photonic density of states. The strength of the diffraction can be adjusted with the filling factor and the depth of the stripes at the backside. Figures 7(b) and 7(c) show the calculated energy flux of the near-field thermal radiation and its SE as functions of the filling factor at $d = 0.1\ \mu$m, where the stripe depth is set to $h = 1\ \mu$m. Here, not only the SE but also the absolute value of the above-bandgap absorption of the PC ($\rho = 0.7$) becomes larger

than those without the PC ($\rho = 1$). Quantitatively speaking, the introduction of the PC ($a = 0.4\,\mu$m, $h = 1\,\mu$m, $\rho = 0.7$) leads to 6% increase both in above-bandgap absorption and SE compared to that without the PC ($\rho = 1.0$). Figure 7(d) shows the above-bandgap absorption power (red line) and the SE (black line) as functions of the stripe depth (ρ is set to 0.7). When the structure has moderately shallow stripes ($h = 0.5 - 1.0\,\mu$m), both the absolute value of the above-bandgap absorption and SE can be boosted compared to those without the PC ($h = 0\,\mu$m).

IV. CONCLUSIONS

We have numerically investigated the near-field thermal radiation transfer between a Si PC emitter and a GaSb absorber and demonstrated that the narrow-bandwidth near-field thermal radiation transfer can be achieved through the careful design of the emitter and absorber. We have revealed that the enhancement of the above-bandgap absorption and the suppression of the below-bandgap emission are compatible when the thicknesses of the emitter and absorber are optimized considering the materials' absorption coefficient spectra. We have also demonstrated that the introduction of a PC slab into the emitter can further increase the frequency selectivity and the absolute power of the near-field thermal radiation transfer when the PC induces selective diffraction of light with the above-bandgap energy, while maintaining the photonic density of states. The methods we propose here (thickness control and introduction of PCs) are universal and thus applicable to other material systems. We believe that our findings will provide important guidelines for the design of high-power high-efficient near-field TPV systems.

ACKNOWLEDGMENTS

This paper was partially supported by Grant-in-Aid for Scientific Research (S) (25220607) from the Japan Society for the Promotion of Science (JSPS) and by the Keihanshin Consortium for Fostering the Next Generation of Global Leaders in Research (K-CONNEX), established by the Human Resource Development Program for Science and Technology, Ministry of Education, Culture, Sports, Science and Technology (MEXT).

APPENDIX A: NUMERICAL SIMULATION OF NEAR-FIELD THERMAL RADIATION TRANSFER BETWEEN PC SLABS

Here, we describe the simulation method of near-field thermal radiation transfer between PC slabs. The method is based on the fluctuation-dissipation theory [25] and the RCWA [26]. Unlike the matrix trace formalism described in previous papers [14,16], our method enables the simulation of a detailed spatial absorption profile in a multilayered structure as well as transmission spectrum through an absorber with a finite thickness.

Two parallel PC slabs (PC1 and PC2) with the same period are opposed to each other, as shown in Fig. 8. The electromagnetic fields of the Bloch mode inside PC1 can be

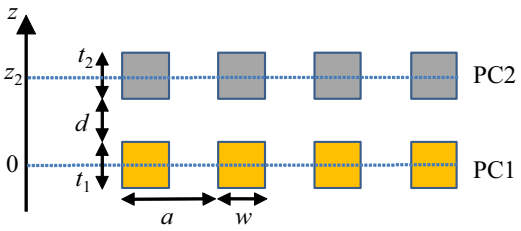

FIG. 8. Simulation model of the near-field thermal radiation transfer between two parallel PC slabs.

written as the superposition of plane waves as follows:

$$\begin{aligned} E_x(\mathbf{r}) &= \exp(i\boldsymbol{\beta}\cdot\boldsymbol{\rho}) \times \sum_n E_{x,n}(z)\exp(i\mathbf{G}_n\cdot\boldsymbol{\rho}) \\ E_y(\mathbf{r}) &= \exp(i\boldsymbol{\beta}\cdot\boldsymbol{\rho}) \times \sum_n E_{y,n}(z)\exp(i\mathbf{G}_n\cdot\boldsymbol{\rho}) \\ H_x(\mathbf{r}) &= \exp(i\boldsymbol{\beta}\cdot\boldsymbol{\rho}) \times \sum_n H_{x,n}(z)\exp(i\mathbf{G}_n\cdot\boldsymbol{\rho}) \\ H_y(\mathbf{r}) &= \exp(i\boldsymbol{\beta}\cdot\boldsymbol{\rho}) \times \sum_n H_{y,n}(z)\exp(i\mathbf{G}_n\cdot\boldsymbol{\rho}), \end{aligned} \tag{A1}$$

where $\mathbf{r} = (x,y,z)$, $\boldsymbol{\rho} = (x,y)$, $\boldsymbol{\beta}$ is the in-plane wave vector of the Bloch mode in the first Brillion zone, and $\mathbf{G}_n$ is the nth reciprocal vector of the PC. Let $\mathbf{E}$ and $\mathbf{H}$ be column vectors that are composed of the expansion coefficients in Eq. (A1)

$$\begin{aligned} \mathbf{E}(z) &= (E_{x,1}, E_{y,1}, E_{x,2}, E_{y,2}, \cdots, E_{x,N}, E_{y,N})^T \\ \mathbf{H}(z) &= (H_{x,1}, H_{y,1}, H_{x,2}, H_{y,2}, \cdots, H_{x,N}, H_{y,N})^T, \end{aligned} \tag{A2}$$

where N is the number of plane waves used for the Fourier expansion. When there are no current sources inside PC1, substituting Eqs. (A1) and (A2) into Maxwell's equations gives the following matrix equations [26]:

$$\frac{\partial}{\partial z}\mathbf{E} = iT_1\mathbf{H}, \quad \frac{\partial}{\partial z}\mathbf{H} = iT_2\mathbf{E}, \tag{A3}$$

$$\frac{\partial^2}{\partial z^2}\mathbf{E} = -T_1T_2\mathbf{E}. \tag{A4}$$

Here, the $2N \times 2N$ matrices T_1 and T_2 are defined as

$$\begin{aligned} T_1^{i,j} &= \frac{1}{\omega\varepsilon_0}\begin{pmatrix} k_{x,i}\varepsilon_{ij}^{-1}k_{y,j} & -k_{x,i}\varepsilon_{ij}^{-1}k_{x,j} + k_0^2\delta_{ij} \\ k_{y,i}\varepsilon_{ij}^{-1}k_{y,j} - k_0^2\delta_{ij} & -k_{y,i}\varepsilon_{ij}^{-1}k_{x,j} \end{pmatrix} \\ T_2^{i,j} &= \frac{1}{\omega\mu_0}\begin{pmatrix} -k_{x,i}\delta_{ij}k_{y,j} & k_{x,i}\delta_{ij}k_{x,j} - k_0^2\varepsilon_{ij} \\ -k_{y,i}\delta_{ij}k_{y,j} + k_0^2\varepsilon_{ij} & k_{y,i}\delta_{ij}k_{x,j} \end{pmatrix}, \end{aligned} \tag{A5}$$

where $k_{x(y),i}$ is the $x(y)$ component of the wave vector of the ith plane wave and ε_{ij} and ε_{ij}^{-1} are the Fourier component of the periodic permittivity distribution

$$\begin{aligned} \varepsilon_{ij} &= \iint_{\text{unitcell}} \varepsilon(\boldsymbol{\rho})\exp[i(\mathbf{G}_i - \mathbf{G}_j)\cdot\boldsymbol{\rho}]d\boldsymbol{\rho}, \\ \varepsilon_{ij}^{-1} &= \iint_{\text{unitcell}} \frac{1}{\varepsilon(\boldsymbol{\rho})}\exp[i(\mathbf{G}_i - \mathbf{G}_j)\cdot\boldsymbol{\rho}]d\boldsymbol{\rho}. \end{aligned} \tag{A6}$$

By defining the eigenvalues and eigenvectors of the matrix T_1T_2 as ${\gamma_i}^2$ ($\mathrm{Im}(\gamma_i) \geqslant 0$) and $\mathbf{u}_i$ ($i = 1, 2, \cdots, 2N$),

Eqs. (A1) and (A2) can be rewritten as

$$\begin{aligned}\mathbf{E}_0(z) &= \mathbf{E}_0{}^{+}(z) + \mathbf{E}_0{}^{-}(z)\\ \mathbf{E}_0{}^{+}(z) &= \sum_i [C_i^{+}\exp(i\gamma_i z)]\,\mathbf{u}_i,\\ \mathbf{E}_0{}^{-}(z) &= \sum_i [C_i^{-}\exp(-i\gamma_i z)]\,\mathbf{u}_i,\end{aligned} \tag{A7}$$

where $\mathbf{E}_0{}^{+}(z)$ and $\mathbf{E}_0{}^{-}(z)$ are the electric field components of the eigenmodes propagating in the $+z$ and $-z$ directions, respectively, and C_i^{+} and C_i^{-} are unknown coefficients.

When PC1 is heated, random fluctuating currents $j_m(\mathbf{r})$ $(m = x,y,z)$ are induced inside the object. According to the fluctuation-dissipation theory, these currents obey the following correlation [6]:

$$\langle j_m(\mathbf{r},\omega) j_{m'}{}^{*}(\mathbf{r}',\omega')\rangle = \frac{4\omega\varepsilon_0 \mathrm{Im}(\varepsilon)}{\pi}\frac{\hbar\omega}{\exp(\hbar\omega/kT)-1} \times \delta_{mm'}\delta(\mathbf{r}-\mathbf{r}')\delta(\omega-\omega'). \tag{A8}$$

As in Eq. (A1), $j_m(\mathbf{r})$ can be expressed with the superposition of plane waves. Using Eq. (A8), the amplitudes of each plane wave $j_{m,n}(z)$ obey the following correlation:

$$\begin{aligned}\langle j_{m,n}(z) j_{m',n'}{}^{*}(z')\rangle &= \frac{1}{16\pi^4}\iint_{\text{unit cell}} d\boldsymbol{\rho}\iint_{\text{unit cell}} d\boldsymbol{\rho}'\langle j_m(\mathbf{r}) j_{m'}{}^{*}(\mathbf{r}')\rangle \exp[i(\mathbf{G}_{n'}\cdot\boldsymbol{\rho}' - \mathbf{G}_n\cdot\boldsymbol{\rho})]\\ &= \frac{\omega\varepsilon_0}{4\pi^5}\frac{\hbar\omega}{\exp(\hbar\omega/kT)-1}\delta_{mm'}\delta(\omega-\omega')\delta(z-z')\iint_{\text{unit cell}} d\boldsymbol{\rho}\mathrm{Im}(\varepsilon)\exp[i(\mathbf{G}_{n'}-\mathbf{G}_n)\cdot\boldsymbol{\rho}].\end{aligned} \tag{A9}$$

When the current sources exist, matrix Eqs. (A3) are modified as follows:

$$\frac{\partial}{\partial z}\mathbf{E} = iT_1\mathbf{H} + \mathbf{J}_1, \quad \frac{\partial}{\partial z}\mathbf{H} = iT_2\mathbf{E} + \mathbf{J}_2, \tag{A10}$$

$$\frac{\partial^2}{\partial z^2}\mathbf{E} = -T_1T_2\mathbf{E} + iT_1\mathbf{J}_2 + \frac{\partial}{\partial z}\mathbf{J}_1, \tag{A11}$$

where

$$\begin{aligned}\mathbf{J}_1 &= \frac{1}{\omega\varepsilon_0}(k_{x,1}(\boldsymbol{\varepsilon}^{-1}\mathbf{j}_z)_1, k_{y,1}(\boldsymbol{\varepsilon}^{-1}\mathbf{j}_z)_1, k_{x,2}\\ &\quad\times(\boldsymbol{\varepsilon}^{-1}\mathbf{j}_z)_2, k_{y,2}(\boldsymbol{\varepsilon}^{-1}\mathbf{j}_z)_2, \cdots)^T\\ \mathbf{J}_2 &= (j_{y,1}, -j_{x,1}, j_{y,2}, -j_{x,2}, \cdots)^T\\ (\boldsymbol{\varepsilon}^{-1}\mathbf{j}_z)_i &= \sum_{j=1}^{N}\varepsilon_{ij}^{-1} j_{z,j}.\end{aligned} \tag{A12}$$

To solve Eq. (A11), we diagonalize the matrix T_1T_2 with its diagonal matrix S_a whose ith row vector is $\mathbf{u}_i$. By multiplying $S_a{}^{-1}$ from the left in Eq. (A11), we obtain

$$\frac{\partial^2}{\partial z^2}S_a^{-1}\mathbf{E} = -S_a^{-1}T_1T_2S_a\left(S_a^{-1}\mathbf{E}\right) + \frac{\partial}{\partial z}S_a^{-1}\mathbf{J}_1 + S_a^{-1}iT_1\mathbf{J}_2. \tag{A13}$$

The equation above can be divided into $2N$ independent differential equations

$$\frac{\partial^2}{\partial z^2}f_i(z) = -\gamma_i^2 f_i(z) + \frac{\partial}{\partial z}p_i(z) + iq_i(z) \times (i = 1, 2, \cdots, 2N), \tag{A14}$$

where $f_i(z), p_i(z), q_i(z)$ are the ith components of the vectors $S_a^{-1}\mathbf{E}, S_a^{-1}\mathbf{J}_1, S_a^{-1}T_1\mathbf{J}_2$, respectively. Here, $f_i(z)$ corresponds to the amplitude of the ith eigenvector $\mathbf{u}_i$. By solving Eq. (A14) using the Fourier method, we obtain

$$f_i(z) = \begin{cases}\frac{\pi}{\gamma_i}[\gamma_i P_i(\gamma_i) + Q_i(\gamma_i)]\exp(i\gamma_i z) & (z>0)\\ \frac{\pi}{\gamma_i}[-\gamma_i P_i(-\gamma_i) + Q_i(-\gamma_i)]\exp(-i\gamma_i z) & (z<0)\end{cases}, \tag{A15}$$

where

$$\begin{aligned}P_i(\gamma_i) &= \frac{1}{2\pi}\int_{-\infty}^{\infty} p_i(z)\exp(i\gamma_i z)dz,\\ Q_i(\gamma_i) &= \frac{1}{2\pi}\int_{-\infty}^{\infty} q_i(z)\exp(i\gamma_i z)dz.\end{aligned} \tag{A16}$$

The integration range of Eq. (A16) can be replaced with $-t_1/2 \leqslant z \leqslant t_1/2$ since the currents are induced only inside the slab. By comparing these results with Eq. (A7), we obtain

$$\begin{aligned}C_i^{+} &= \frac{\pi}{\gamma_i}[\gamma_i P_i(\gamma_i) + Q_i(\gamma_i)],\\ C_i^{-} &= \frac{\pi}{\gamma_i}[-\gamma_i P_i(-\gamma_i) + Q_i(-\gamma_i)].\end{aligned} \tag{A17}$$

The plane waves excited by the fluctuation currents at the reference plane $(z = 0)$ inside PC1 then propagate to PC2 while receiving multiple reflections. The electromagnetic fields at the observation plane $(z = z_2)$ inside PC2 can be expressed as

$$\begin{aligned}\mathbf{E}_2 &= \sum_i [M_E^{+}C_i^{+}\mathbf{u}_i + M_E^{-}C_i^{-}\mathbf{u}_i]\\ \mathbf{H}_2 &= \sum_i [M_H^{+}C_i^{+}\mathbf{u}_i + M_H^{-}C_i^{-}\mathbf{u}_i].\end{aligned} \tag{A18}$$

Here, $M_E^{\pm}, M_H^{\pm}$ are the transfer matrices for the plane waves from the reference plane in PC1 to the observation plane in PC2, which can be calculated using the RCWA method [26]. Finally, the spectral energy flux propagating through the observation plane inside PC2 is given by the

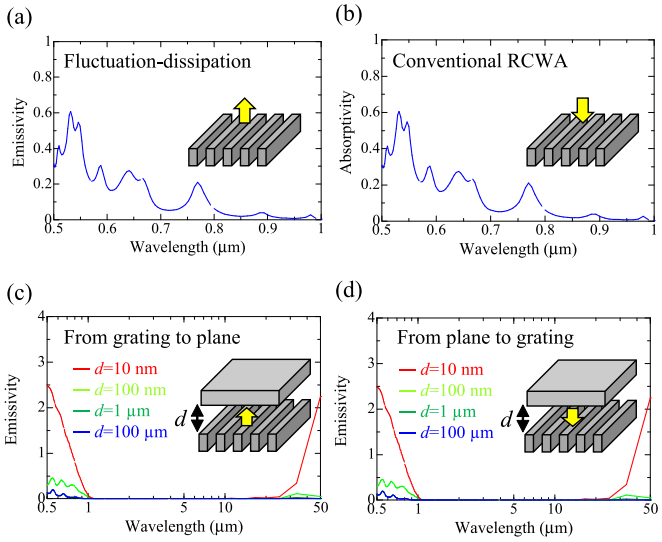

FIG. 9. Far-field emissivity spectrum of a one-dimensional Si grating ($a = 0.5\,\mu$m, $t = 0.5\,\mu$m, $w = 0.25\,\mu$m) in the normal direction, calculated using (a) the fluctuation-dissipation method and (b) the conventional RCWA. (c) and (d) Near-field thermal radiation transfer spectrum (normalized by the far-field blackbody spectrum) from a Si grating ($a = 0.5\,\mu$m, $t = 0.5\,\mu$m, $w = 0.25\,\mu$m) to a Si plane ($t = 0.5\,\mu$m) and that from the Si plane to the Si grating.

summation of the Poynting vectors for all in-plane wave vectors

$$S(\omega) = \int_{\text{1stBrillouin}} d\boldsymbol{\beta}\ \frac{1}{2}\text{Re}\left[\left\langle \sum_{n=1}^{N} \left(E_{2x,n} H_{2y,n} - E_{2y,n} H_{2x,n}\right)\right\rangle\right]. \tag{A19}$$

The calculation of the summation can be performed by substituting Eqs. (A12), (A16)–(A18) into Eq. (A19), expanding the summation, and using the correlation of the fluctuation currents [Eq. (A9)] for each term.

To confirm the validity of our method, we perform two simulation tests. In the first test, we calculate the far-field emissivity spectrum of a one-dimensional Si grating ($a = 0.5\,\mu$m, $t = 0.5\,\mu$m, and $w = 0.25\,\mu$m) in the normal direction using the abovementioned method and compare it with the far-field absorptivity spectrum of the same grating in the normal direction calculated with the conventional RCWA program. The results are shown in Figs. 9(a) and 9(b), where both spectra completely agree with each other. In the second test, we check the duality of our simulation program by comparing the near-field thermal radiation transfer spectrum (normalized by the far-field blackbody spectrum) from a Si grating ($a = 0.5\,\mu$m, $t = 0.5\,\mu$m, $w = 0.25\,\mu$m) to a Si plane ($t = 0.5\,\mu$m) with that from the Si plane to the Si grating. The obtained results are the same as shown in Figs. 9(c) and 9(d), indicating the validity of our simulation method.

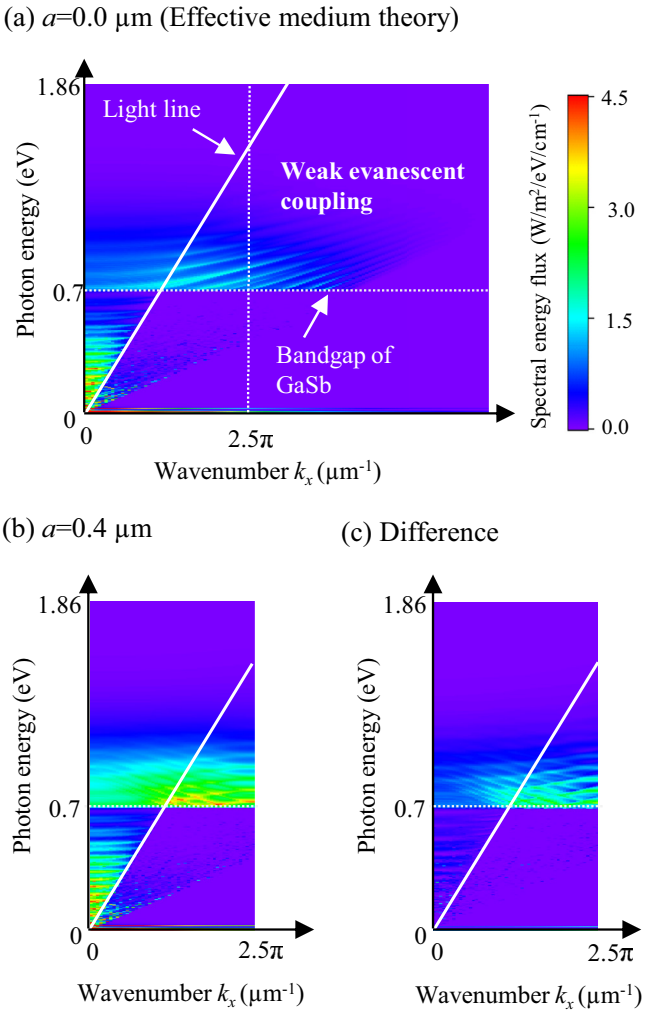

FIG. 10. Wavenumber-resolved near-field thermal radiation transfer spectrum between a Si PC emitter ($t_1 = 2\,\mu$m and $\rho = 0.9$) and a GaSb absorber ($t_2 = 2\,\mu$m) at the gap $d = 0.1\,\mu$m. The lattice constant of the PC is (a) $a = 0.2\,\mu$m and (b) $a = 0.4\,\mu$m. (c) Difference between (b) and (a) in the wavenumber range of $0 < k_x < 2.5\pi\ \mu$m^{-1}. The band-folding effect selectively enhances the thermal radiation transfer in the above-bandgap energy.

APPENDIX B: SELECTIVE NEAR-FIELD THERMAL RADIATION TRANSFER USING THE BAND-FOLDING EFFECT IN PC SLABS

In this appendix, we show additional calculation results in order to quantitatively affirm the mechanism of selective near-field thermal radiation transfer in PCs. Figure 10 shows the wavenumber-resolved near-field thermal radiation transfer spectrum between a Si PC emitter ($t_1 = 2\,\mu$m and $\rho = 0.9$) and a GaSb absorber ($t_1 = 2\,\mu$m) at the gap $d = 0.1\,\mu$m [corresponding to Figs. 6(a) and 6(b)]. The lattice constant of the PC is set to $a = 0\,\mu$m in Fig. 10(a) (calculated by the EMT) and $a = 0.4\,\mu$m in Fig. 10(b). In Fig. 10(a), the modes far away from the light line ($k_x > 2.5\pi\ \mu$m^{-1}) contribute less to the near-field thermal radiation transfer. When the PC is introduced [Fig. 10(b)], the above-bandgap thermal radiation in the range of the first Brillouin zone ($0 < k_x < 2.5\pi\ \mu$m^{-1}) is drastically enhanced. The difference between (b) and (a)

in the wavenumber range of $0 < k_x < 2.5\pi\ \mu\text{m}^{-1}$ is shown in Fig. 10(c), which clearly indicates that the folding of the photonic band is the key to realize selective enhancement of the thermal radiation transfer in the above-bandgap energy.

[1] D. Polder and M. V. Hove, Theory of radiative heat transfer between closely spaced bodies, Phys. Rev. B **4**, 3303 (1971).

[2] J. J. Loomis and H. J. Maris, Theory of heat transfer by evanescent electromagnetic waves, Phys. Rev. B **50**, 18517 (1994).

[3] K. Joulain, J.-P. Mulet, F. Marquier, R. Carminati, and J.-J. Greffet, Surface electromagnetic waves thermally excited: Radiative heat transfer, coherence properties and Casimir forces revisited in the near field, Surf. Sci. Rep. **57**, 59 (2005).

[4] M. Laroche, R. Carminati, and J.-J. Greffet, Near-field thermophotovoltaic energy conversion, J. Appl. Phys. **100**, 063704 (2006).

[5] K. Park, S. Basu, W. P. King, and Z. M. Zhang, Performance analysis of near-field thermophotovoltaic devices considering absorption distribution, J. Quant. Spectrosc. Radiat. Transfer **109**, 305 (2008).

[6] S. Basu, Z. M. Zhang, and C. J. Fu, Review of near-field thermal radiation and its application to energy conversion, Int. J. Energy Res. **33**, 1203 (2009).

[7] O. Ilic, M. Jablan, J. D. Joannopoulos, I. Celanovic, and M. Soljačić, Overcoming the black body limit in plasmonic and graphene near-field thermophotovoltaic systems, Opt. Express **20**, A366 (2012).

[8] J. K. Tong, W.-C. Hsu, Y. Huang, S. V. Boriskina, and G. Chen, Thin-film 'thermal well' emitters and absorbers for high-efficiency thermophotovoltaics, Sci. Reports **5**, 10661 (2015).

[9] C. R. Otey, W. T. Lau, and S. Fan, Thermal Rectification through Vacuum, Phys. Rev. Lett. **104**, 154301 (2010).

[10] S. Basu and M. Francoeur, Near-field radiative transfer based thermal rectification using doped silicon, Appl. Phys. Lett. **98**, 113106 (2011).

[11] C. J. Fu and Z. M. Zhang, Nanoscale radiation heat transfer for silicon at different doping levels, Int. J. Heat Mass Transfer **49**, 1703 (2006).

[12] P. Ben-Abdallah, K. Joulain, J. Drevillon, and G. Domingues, Near-field heat transfer mediated by surface wave hybridization between two films, J. Appl. Phys. **106**, 044306 (2009).

[13] A. W. Rodriguez, O. Ilic, P. Bermel, I. Celanovic, J. D. Joannopoulos, M. Soljačić, and S. G. Johnson, Frequency-Selective Near-Field Radiative Heat Transfer between Photonic Crystal Slabs: A Computational Approach for Arbitrary Geometries and Materials, Phys. Rev. Lett. **107**, 114302 (2011).

[14] R. Guérout, J. Lussange, F. S. S. Rosa, J.-P. Hugonin, D. A. R. Dalvit, J.-J. Greffet, A. Lambrecht, and S. Reynaud, Enhanced radiative heat transfer between nanostructured gold plates, Phys. Rev. B **85**, 180301(R) (2012).

[15] Y. Guo, C. L. Cortes, S. Molesky, and Z. Jacob, Broadband super-Planckian thermal emission from hyperbolic metamaterials, Appl. Phys. Lett. **101**, 131106 (2012).

[16] X. L. Liu and Z. M. Zhang, Graphene-assisted near-field radiative heat transfer between corrugated polar materials, Appl. Phys. Lett. **104**, 251911 (2014).

[17] H. Chalabi, E. Hasman, and M. L. Brongersma, Near-field radiative thermal transfer between a nanostructured periodic material and a planar substrate, Phys. Rev. B **91**, 014302 (2015).

[18] X. L. Liu and Z. M. Zhang, Near-field thermal radiation between metasurfaces, ACS Photonics **2**, 1320 (2015).

[19] M. D. Zoysa, T. Asano, K. Mochizuki, A. Oskooi, T. Inoue, and S. Noda, Conversion of broadband to narrowband thermal emission through energy recycling, Nature Photon. **6**, 535 (2012).

[20] T. Inoue, M. D. Zoysa, T. Asano, and S. Noda, Single-peak narrow-bandwidth mid-infrared thermal emitters based on quantum wells and photonic crystals, Appl. Phys. Lett. **102**, 191110 (2013).

[21] T. Inoue, M. D. Zoysa, T. Asano, and S. Noda, Realization of dynamic thermal emission control, Nat. Mater. **13**, 928 (2014).

[22] P. J. Timan, Emissivity of silicon at elevated temperatures, J. Appl. Phys. **74**, 6353 (1993).

[23] S. Adachi, *Optical Constants of Crystalline and Amorphous Semiconductors* (Springer Science and Business Media, New York, 2013).

[24] M. Patrini, G. Guizzetti, M. Galli, R. Ferrini, A. Bosacchi, S. Franchi, and R. Magnanini, Optical functions of bulk and epitaxial GaSb from 0.0025 to 6 eV, Solid State Commun. **101**, 93 (1997).

[25] S. M. Rytov, Y. A. Kravtsov, and V. I. Tatarskii, *Principles of Statistical Radiophysics*, Vol. 3 (Springer-Verlag, Berlin, Heidelberg, 1989).

[26] L.-L. Lin, Z.-Y. Li, and K.-M. Ho, Lattice symmetry applied in transfer-matrix methods for photonic crystals, J. Appl. Phys. **94**, 811 (2003).